

Coherent control of an ultrabright single spin in hexagonal boron nitride at room temperature

Received: 13 September 2022

Accepted: 10 May 2023

Published online: 20 May 2023

 Check for updates

Nai-Jie Guo^{1,2,3,7}, Song Li^{4,7}, Wei Liu^{1,2,3,7}, Yuan-Ze Yang^{1,2,3,7}, Xiao-Dong Zeng^{1,2,3,7}, Shang Yu^{1,2,3}, Yu Meng^{1,2,3}, Zhi-Peng Li^{1,2,3}, Zhao-An Wang^{1,2,3}, Lin-Ke Xie^{1,2,3}, Rong-Chun Ge⁵, Jun-Feng Wang^{1,2,3,5}, Qiang Li^{1,2,3}, Jin-Shi Xu^{1,2,3}, Yi-Tao Wang^{1,2,3}✉, Jian-Shun Tang^{1,2,3}✉, Adam Gali^{1,2,3}✉, Chuan-Feng Li^{1,2,3}✉ & Guang-Can Guo^{1,2,3}

Hexagonal boron nitride (hBN) is a remarkable two-dimensional (2D) material that hosts solid-state spins and has great potential to be used in quantum information applications, including quantum networks. However, in this application, both the optical and spin properties are crucial for single spins but have not yet been discovered simultaneously for hBN spins. Here, we realize an efficient method for arraying and isolating the single defects of hBN and use this method to discover a new spin defect with a high probability of 85%. This single defect exhibits outstanding optical properties and an optically controllable spin, as indicated by the observed significant Rabi oscillation and Hahn echo experiments at room temperature. First principles calculations indicate that complexes of carbon and oxygen dopants may be the origin of the single spin defects. This provides a possibility for further addressing spins that can be optically controlled.

Solid-state spin defects play a crucial role in quantum information applications¹, especially color-center defects that have electronic spins that can be optically initialized and provide readouts, such as the nitrogen-vacancy (NV) center in diamond² and the divacancy defect in silicon carbide³. The coherent control of these spin defects is possible even under ambient conditions (e.g., room temperature and normal atmosphere)⁴. Hence, they are practical resources in the construction of room-temperature spintronic quantum devices⁵. Furthermore, an individual solid-state spin defect exhibits the characteristics of single-photon emission and nanoscale spatial resolution, and it is critical for various quantum-information applications, such as quantum photon source⁶, nanoscale quantum

sensors⁷, and quantum networks⁸. Especially in quantum networks, photon-spin entanglement and coupling play crucial roles. To achieve these aims, both the optical and spin performances are needed for this single spin.

Recently, hexagonal boron nitride (hBN) has attracted considerable attention as a wide-band-gap van der Waals material that can host color-center spin defects⁹. The spin defects in hBN benefit from the unique physical properties of van der Waals materials, e.g., flexible mechanical properties and natural two-dimensional characteristics; hence, they possess multiple modulation mechanisms and have great potential to be applied in the fabrication of two-dimensional quantum devices and integrated quantum nanodevices^{10–13}.

¹CAS Key Laboratory of Quantum Information, University of Science and Technology of China, Hefei, Anhui 230026, China. ²CAS Center For Excellence in Quantum Information and Quantum Physics, University of Science and Technology of China, Hefei, Anhui 230026, China. ³Hefei National Laboratory, University of Science and Technology of China, Hefei 230088, China. ⁴Wigner Research Centre for Physics, Post Office Box 49 H-1525 Budapest, Hungary. ⁵College of Physics, Sichuan University, Chengdu 610064, China. ⁶Department of Atomic Physics, Institute of Physics, Budapest University of Technology and Economics, Muegyetem rakpart 3 H-1111 Budapest, Hungary. ⁷These authors contributed equally: Nai-Jie Guo, Song Li, Wei Liu, Yuan-Ze Yang, Xiao-Dong Zeng. ✉ e-mail: yitao@ustc.edu.cn; tjs@ustc.edu.cn; gali.adam@wigner.hu; cfl@ustc.edu.cn

The discovered spin defects in hBN include the negatively charged boron vacancy (V_B^-) defect^{14–26} and several carbon-related defects^{27–29}. At room temperature, the spin state of the V_B^- defect exhibits obvious contrast under optically detected magnetic resonance (ODMR)³⁰ and Rabi oscillation with microwave (MW) resonance^{31,32}. This indicates that the optical initialization/readout and coherent control of V_B^- in hBN are possible under the ambient conditions, but this is only possible for the ensemble. The isolation of a single V_B^- defect is still challenging due to its poor optical properties. Compared to other color-center defects, V_B^- defects in hBN display extremely low-quantum efficiency for the optical transition. This low-quantum-efficiency characteristic makes it difficult to detect a single V_B^- defect, although many studies have succeeded in effectively enhancing the photoluminescence (PL) of the V_B^- defect^{30,33,34}. In addition, the PL of V_B^- always exhibits a broad spectrum with a considerable phonon sideband (PSB), even in the liquid-helium temperature region, and the zero-phonon-line (ZPL) does not appear. For some other defects in hBN, single spins with ODMR are found, but the probability is too low (~5%²⁹). Considering the low probability of detecting the Rabi signal (10.5%, see data in Table 2), it is difficult to observe the obvious coherent control of a single spin. In addition, other optical properties of these defects, for example, the Debye-Waller (DW) factor, still have room for improvement. These problems hinder the room-temperature quantum control of a single spin with good optical performance in hBN, which is crucial for quantum information applications based on solid-state spin defects.

Here, we experimentally demonstrate an effective method for generating the color-center array of hBN on a gold-film MW waveguide and enhance the probability of finding a single spin with an ODMR (85%) by 21-fold. Based on this progress, we realize the room-temperature coherent control of a single spin defect in hBN. We discover a new single spin in this array, which has both outstanding optical and spin properties that can potentially be used in quantum information applications. This defect has $g^{(2)}(0) = 0.25$, an emission rate of 25 MHz (corrected), a DW factor of 0.8, an ODMR contrast of 2%, a linewidth of 22 MHz, clear Rabi oscillation, and $T_1 = 16.17 \mu\text{s}$ and $T_2 = 2.45 \mu\text{s}$ (from Hahn-echo experiment). The values of T_1 and T_2 reach the level of the V_B^- defect. We also carried out ab initio simulations, and the results imply that this new defect may be a complex of carbon and oxygen dopants.

Results

Color-center array

To generate the color-center array of hBN, we use electron beam lithography to produce hole-array patterning on a silicon dioxide substrate coated with polymethyl methacrylate (PMMA) resist, and suspend the dispersed hBN ultrafine powder in the holes by capillary force^{35–37}. The PMMA resist is subsequently dissolved, leaving the hBN-flake array on the gold film MW waveguide, as shown in Fig. 1. The gold

film MW waveguide fabricated by photolithography under the spin-defect array can provide a uniform and stable local MW field and enhance the quantum efficiency and reflection efficiency of the spin defect^{22,23,30}. The scanning electron microscope (SEM) image of the hBN nanoflake in a single hole of the array is shown in Fig. 1c, showing that the single hBN flake can be isolated effectively. The hBN flakes originally host optically active defects^{38–43}, and this process increases the possibility of isolating a single nanoflake with a single spin defect instead of a cluster of flakes. See the experimental section for details on the sample preparation process.

The confocal PL map of the hBN array is shown in Fig. 2a, which is scanned by a home-built confocal microscope. Defect A is obviously brighter than the other defects, and we perform the characterizations mainly on Defect A, as reported in the following.

Optical properties

The room-temperature PL spectrum of Defect A is shown in Fig. 2b, with a ZPL at -546 nm (which is coincident with the theoretical prediction; See Supplementary Fig. 6) and full width at half maximum (FWHM) = 6.5 nm. A weak PSB peak is located at -588 nm corresponding to the 162-meV phonon. The DW factor, defined as the ratio of the integrated intensity of the ZPL to the total intensity of the emission, is derived as -0.8. This DW factor indicates weak electron-phonon coupling and is one of the highest values of the reported quantum emitters in hBN at room temperature⁴⁴. The emission polarization behaviors of Defect A are shown in Fig. 2d, where the degree of polarization (DOP) equals to -0.8, which is consistent with the characteristic of a single linearly polarized dipole. The emission stability of Defect A is shown in Fig. 2f, exhibiting stable fluorescence emission with no significant blinking over 400 s, and we also do not observe the bleaching effect of this defect during data measurement.

We also perform the second-order autocorrelation measurement for the photons emitted from Defect A at 100- μW laser power. The result is shown in Fig. 2c where $g^{(2)}(0) = 0.25 \pm 0.02 < 0.5$, indicating that Defect A acts as a single-photon emitter. The PL counts of Defect A are presented in Fig. 2e. The emission rate under continuous excitation and excitation power at saturation are $I_{\text{sat}} = 3.7 \pm 0.20$ MHz and $P_{\text{sat}} = 446 \pm 54 \mu\text{W}$, respectively. When taking the collection and detection efficiency into consideration, the corrected saturation emission rate can reach 25 MHz (See Supplementary Note 1 for details). The above optical properties of a high DW factor, high DOP, and high optical stability reveal that the trapping-electron state in Defect A is hardly disturbed by the surroundings, and the optical properties of low $g^{(2)}(0)$ and high brightness suggest that Defect A is a single optically active defect, possibly with high quantum efficiency.

ODMR measurements

To determine whether Defect A has a spin that can be optically initialized and detected, we perform ODMR measurements under 100- μW ,

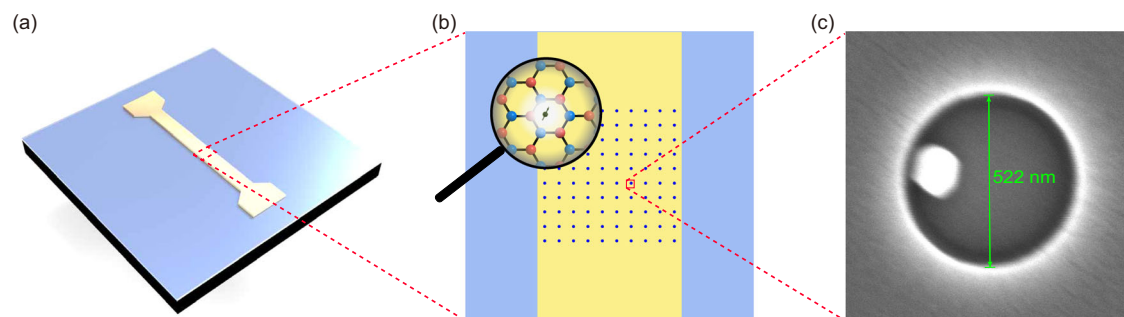


Fig. 1 | Schematic of hBN arrays on the gold film MW waveguide. **a** A schematic of a gold film MW waveguide on silicon wafer generating a uniform and stable local MW field. **b** A schematic of hBN arrays by dispersing the hBN suspension into the

holes formed by electron beam lithography. Inset: Schematic of the atomic structure of hBN. **c** Scanning electron microscope image of an isolated hBN flake in one hole of the array before the PMMA resist was dissolved.

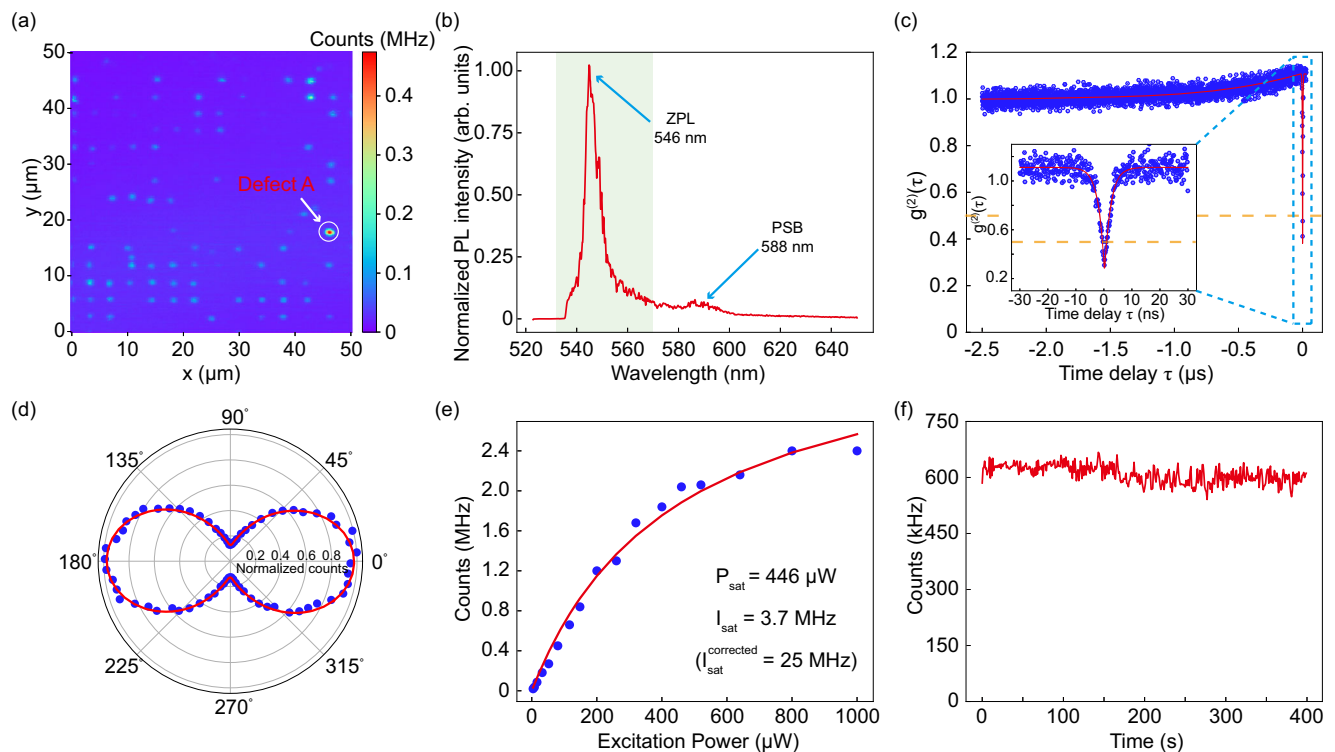


Fig. 2 | Optical properties of the single spin in hBN. **a** $50 \times 50\text{-}\mu\text{m}^2$ confocal PL map of hBN arrays with $100\text{-}\mu\text{W}$ laser excitation at 532 nm . Our measurements correspond to the ultrabright single spin of Defect A circled in the image. **b** Room-temperature photoluminescence spectrum of Defect A under 532-nm laser excitation and with a 532-nm longpass filter. The zero-phonon line (ZPL) is indicated by green bands and the phonon sideband (PSB) is located at 588 nm . **c** Second-order autocorrelation measurement $g^{(2)}(\tau)$ of Defect A, which is measured at $100\text{-}\mu\text{W}$ laser power. The blue dots are the experimental data, the red curve is a fit based on the

three-state model, and the yellow line represents $g^{(2)}(\tau) = 0.5$. Inset: A zoom of the same measurement for short timescales indicates the fitted $g^{(2)}(0) = 0.25 \pm 0.02$. **d** Emission (blue dots) polarization behaviors of Defect A. The red curve is fitted using a $\cos^2\theta$ function. **e** Saturation curve of Defect A under 532-nm laser excitation. "Corrected" means that the saturated intensity is corrected by the photon collecting and detecting efficiencies. See Supplementary Note 1. **f** Time-dependence of photoluminescence counts of Defect A, showing stable emission from Defect A.

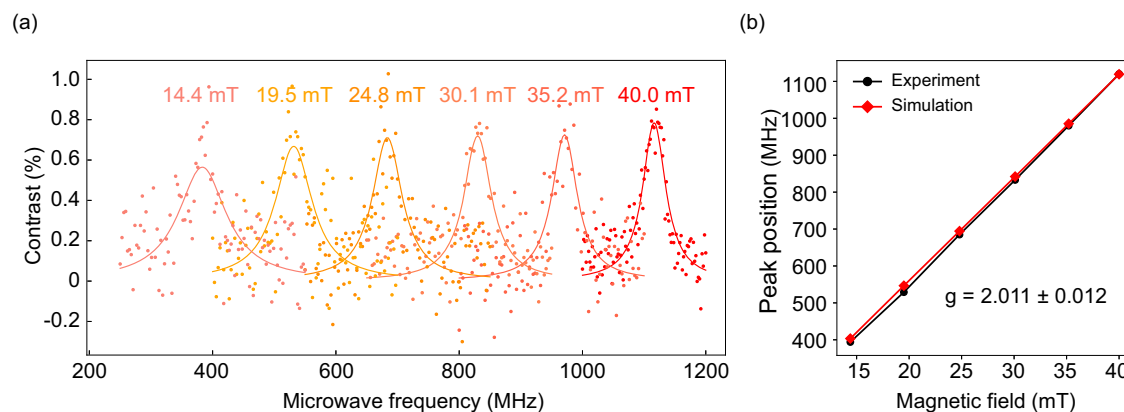


Fig. 3 | Optically detected electron spin resonance of Defect A at room temperature under $100\text{-}\mu\text{W}$ laser excitation and 25-dBm MW power. **a** ODMR spectra of Defect A measured at different external magnetic field. **b** Dependence of

ODMR resonance frequencies on the magnetic field ($\mathbf{B} \parallel \mathbf{c}$). The black dots are experimental results extracted from (a), based on which we fit the g factor of Defect A to be 2.011 ± 0.012 . The red dots are ab initio theoretical predictions.

532-nm laser excitation, and 25-dBm MW power. The results are shown in Fig. 3. An electromagnet is used to provide the variable and controllable external magnetic field parallel to the hexagonal c axis ($\mathbf{B} \parallel \mathbf{c}$) of hBN. The ODMR spectra with the single positive peak of Defect A at the different magnetic fields are displayed in Fig. 3a. As the magnetic field intensity decreases, the ODMR contrast decreases slightly and the linewidth increases slightly (we note that this may be caused by the decreasing signal-to-noise ratio, which impacts the fitting results of

these ODMR spectra; in the following experiment, we will show that the linewidth is only dependent on the laser and MW powers.). The ODMR positive peak exhibits a contrast of 0.8% and a linewidth of 37 MHz under the current laser and MW powers for the 40-mT data, which has the highest signal-to-noise ratio. The relation of the ODMR peak position and the magnetic-field strength is shown in Fig. 3b, which is coincident with the ab initio theoretical prediction, and from these data, we can fit the g -factor close to 2 for this spin state.

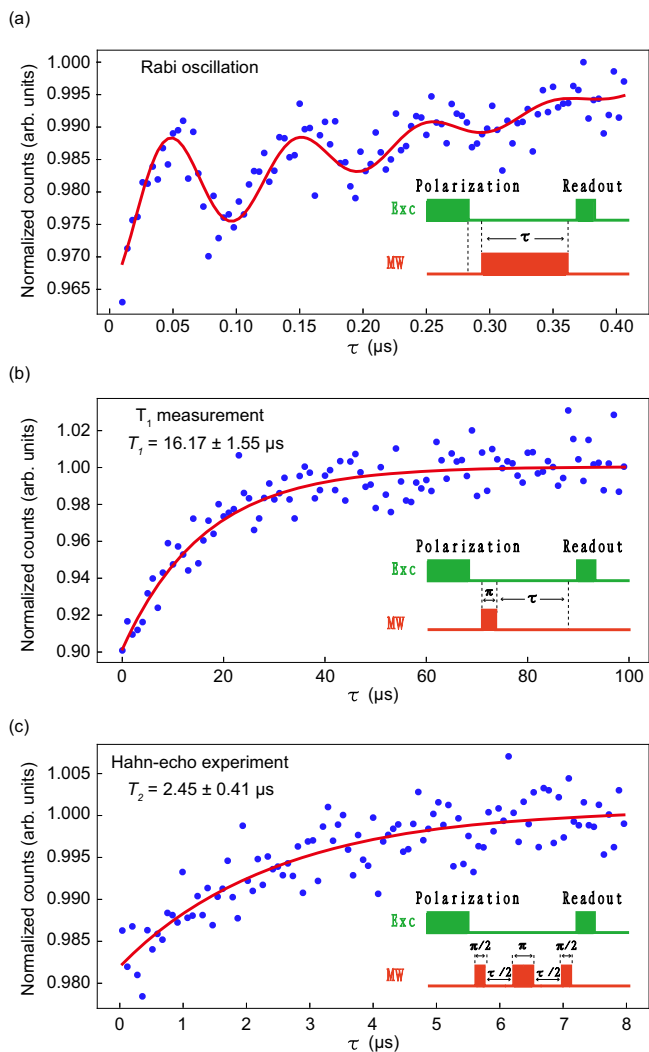


Fig. 4 | Room-temperature coherent spin manipulation of Defect A. **a** Rabi oscillation of Defect A. The inset schematically shows the pulse sequence, in which the first excitation laser pulse is used for the initialization of the spin state and the second pulse is used for a readout of the state after the MW pulse. **b** Spin-lattice relaxation time (T_1) measurement of Defect A. The inset schematically shows the pulse sequence, in which the duration of the MW π -pulse is obtained from Rabi oscillation and the waiting time τ is varied. We can obtain the fitted $T_1 = 16.17 \pm 1.55 \mu\text{s}$. **c** Hahn-echo experiment of Defect A. The inset schematically shows the pulse sequence. We can obtain the fitted $T_2 = 2.45 \pm 0.41 \mu\text{s}$. All measurements are performed under a 35.8-mT magnetic field at room temperature.

Room-temperature coherent control

Next, we demonstrate the room-temperature coherent control of the single spin of Defect A in hBN. The pulsed ODMR is applied at the 35.8-mT magnetic field to manipulate the spin state, and the results are shown in Fig. 4. We first polarize the spin state to the ground state by optical excitation and then apply a MW pulse with variable lengths whose frequency is resonant with the spin-level splitting, followed by another laser pulse for the readout of the spin state. This is the process of Rabi-oscillation measurement, and the pulse sequence and result of Defect A are shown in Fig. 4a. This result is fitted by the Equation $A + Be^{-\tau/T_2} \cos(2\pi f\tau + \phi) + Ce^{-\tau/T_0}$. The spin-dephasing time T_2 obtained from the exponential decay of the oscillation term is -140 ns. To determine the spin relaxation times T_1 and T_2 of Defect A, we perform T_1 measurements and Hahn-echo experiments. The pulse sequences are shown as insets in Fig. 4b, c, where the parameters of π -pulse and $\pi/2$ -pulse are obtained from the results of Rabi oscillation. The results of the spin-lattice relaxation time T_1 and spin-spin relaxation time T_2 are shown in the corresponding main figures, where T_1 and T_2 are derived as -16.17 μs and -2.45 μs , respectively.

Discussion

We compare Defect A with the other spin defects reported in hBN, as shown in Table 1. The ultrabright and photostable single spin Defect A with the ZPL at -546 nm is significantly different from the other reported spin defects and exhibits the highest brightness and DW factor among these defects. The excellent optical properties can lead to high-efficiency optical initiation and readout of the spin with a high signal-to-noise ratio and are helpful for the further realization of the spin-photon interface based on the two-dimensional van der Waals material of hBN. The spin relaxation times T_1 - 16.17 μs and T_2 - 2.45 μs of Defect A are comparable to those of the V_B^- ensemble at room temperature³¹, which has the longest T_2 time of hBN among those reported. The room-temperature optical and spin properties, including the coherent control of the single spin defect in hBN, indicate that it can indeed be potentially applied in practical quantum-information applications in the future.

Theoretical simulation

To explore the structure of Defect A, we vary the magnetic field, laser power and microwave power to perform ODMR measurements (see Supplementary Note 3). Figure 5 shows the dependence of the ODMR linewidth on the magnetic field, laser power and microwave power, indicating that the linewidth has almost no dependence on the magnetic field and exhibits a power-broadening effect. Regrettably, no obvious hyperfine structure can be observed even at very low laser power and microwave power, which might indicate relatively strong internuclear interactions among neighboring boron and nitrogen atoms mediated by the electron wavefunction.

Table 1 | The results of comparing our defects with reported spin defects

	$g^{(2)}(0)$	Saturated counts	ZPL	DW factor	DOP	Coherent control	T_1 (room/cryogenic)	T_2 (room/cryogenic)
V_B^- (ensemble)	-	-	-	-	-	Yes	18 μs /12.5 ms ³¹	2 μs /2 μs ³¹
Mendelson et al. ²⁸ (ensemble)	-	-	585 nm	-	-	-	- / -	- / -
Stern et al. ²⁹	0.34	$3.8 \times 10^4 \text{ s}^{-1}$	~580 nm	-	-	-	- / -	- / -
Chejanovsky et al. ²⁷	0.59	-	720 nm	-	-	-	- / 17 μs	- / -
	0.22	-	760 nm	-	-	-	- / 13 μs	- / -
Guo et al. ^a	0.25	$3.7 \times 10^6 \text{ s}^{-1}$ $2.5 \times 10^7 \text{ s}^{-1}$ (corrected)	~540 nm	0.8	0.8	Yes	16.17 μs /not detected	2.45 μs /not detected

$g^{(2)}(0)$ is the second-order autocorrelation measurement, ZPL is zero-phonon line, DOP is the degree of polarization.

^aResults in current work.

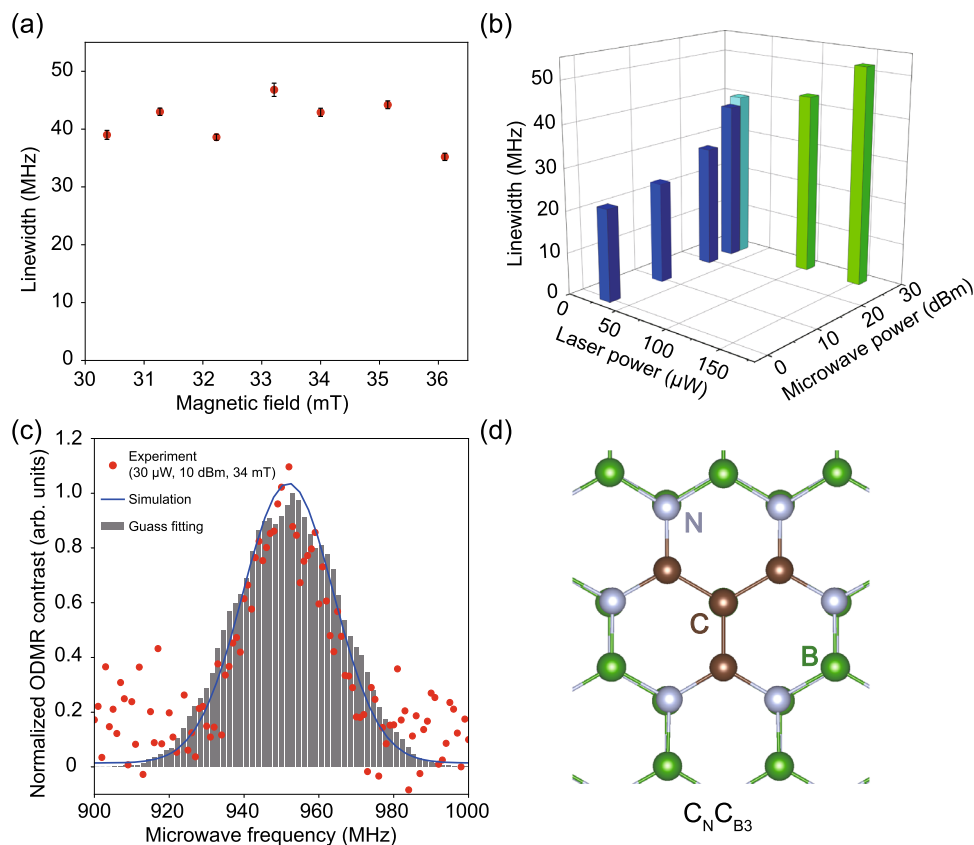


Fig. 5 | ODMR linewidth analysis for Defect A. **a** Dependence of the ODMR linewidth on the magnetic field. The error bars correspond to the fitting errors. The measurements are performed at 100- μ W laser power and 25-dBm microwave power at room temperature. **b** Dependence of the ODMR linewidth on laser power

and microwave power. The measurements are performed under a 34-mT magnetic field at room temperature. **c** Comparison between the simulated and experimental ODMR signals with $C_N C_{B3}$ model. **d** Schematic structure of the defect $C_N C_{B3}$ in hBN.

We apply low-power lasers and microwaves to decrease the power-broadening effect and reduce nuclear spin polarization. The observed linewidth is approximately 22 MHz (Fig. 5b with 30- μ W laser and 0-dBm MW powers). Experimentally, it is a challenge to identify the atomic structure of defect emitters. Theoretical models can be developed using density functional theory calculations, and the simulated key parameters, including ZPL, PSB, and ODMR broadening caused by the hyperfine interaction between the electron spin and nuclear spins, can be directly compared to experimental values to identify defect. A previous investigation assigned carbon-substituted boron (C_B) as a single defect spin with a FWHM of the ODMR spectrum of \sim 43 MHz⁴⁵. However, the calculated ZPL of C_B is 731 nm (1.695 eV) which does not coincide with the observed ZPL of Defect A (\sim 546 nm), even considering the anticipated inaccuracy of 0.2 eV in the applied method⁴⁵. Considering the similar ODMR spectra of that ODMR center²⁷ and Defect A in our study, our working model is a complex consisting of C_B defects in which the spin density should be localized on C_B with an $S = 1/2$ spin state. The relatively narrow ODMR linewidth in the experiment is related to the spin density localization on either nuclear spin-free isotopes with high natural abundance or nuclear spin isotopes with small gyromagnetic ratio, which is followed by the spin density overlapping with neighboring boron and nitrogen atoms with nonzero nuclear spins. The likely impurity candidates are carbon, oxygen and silicon^{46,47}. Among the possible structures, the positively charged $C_B O_N$ pair defect with C_{2v} symmetry could be a reasonable model. The calculated ZPL of $C_B O_N$ is 538 nm (2.303 eV), and the Huang-Rhys (HR) factor S is 2.58. We further calculate the hyperfine tensor of nuclear spins proximate to the $C_B O_N$ to simulate the broadening of the ODMR signal under varying external magnetic fields. A

detailed discussion can be found in Supplementary Note 7. The peak position agrees well with the experimental result (Fig. 3b). The FWHM is approximately 23 MHz, slightly larger than the observed FWHM at low laser and MW powers when considering ^{13}B isotopes. However, the C_{2v} structure is not the most stable, and we observe a C_{1h} symmetry configuration with carbon atoms moving out-of-plane. As a consequence, the ODMR linewidth increases to 50 MHz due to the localized wavefunction partially transferring to nitrogen atoms interacting with their nuclear spins. In addition, the C_B and O_N defects are both donors⁴⁸ in hBN so that the $C_B O_N$ complex has a high formation energy due to repulsion. Based on these findings, we further seek possible defects with a narrow ODMR linewidth in the stable ground state^{49,50}. One facile treatment is to substitute the nearest boron (nitrogen) atoms close to C_N (C_B), resulting in a carbon cluster, which may then result in a planar geometric configuration. $C_2 C_B$ has an ODMR width of approximately 27 MHz, but the ZPL is much less than the current value^{45,51}. Here, we propose a $C_N C_{B3}$ defect^{52,53} in which the C_N is surrounded by three C_B atoms, as shown in Fig. 5d. The positively charged $C_N C_{B3}$ shows a ZPL at 675.4 nm (1.836 eV) with $S = 1.51$ (see Supplementary Note 7 for the $C_N C_{B3}$ details). The ODMR linewidth at 28 MHz in the electronic ground state implies that this defect configuration is a part of defect A. We further note that interlayer impurity oxygen interstitial is also considered (see Supplementary Note 7). The interlayer interstitial atom attracts atoms from the top and bottom layers, resulting in a distorted geometry of the sp^3 bonding configuration. This again leads to a relatively large hyperfine interaction with neighboring boron and nitrogen atoms; therefore, it is likely that defect A is a planar defect similar to $C_N C_{B3}$. Although the exact structure of the defect is not identified here, our results strongly imply that the configurations of

Table 2 | Statistics on the probability of finding a single spin defect

	Total defects investigated	Isolated defects	Isolated defects with ODMR signal	P ₁	P ₂	P ₃
Stern et al. ²⁹	–	More than 400	27	–	~5%	–
Spin-coated sample	50	13	2	4%	15.4%	10.5%
Isolated-flake-array sample	20	20	17	85%	85%	

The total defects in our work are screened out by the brightness threshold. P₁ is the ratio of isolated defects with ODMR signal to the Total defects investigated, P₂ is the ratio of isolated defects with ODMR signal to all the isolated defects, and P₃ is the ratio of isolated defects with evident Rabi oscillations to the isolated defects with ODMR signal.

the substituted carbon and oxygen impurities play the key rule, where the spin density is mostly localized on the p_z orbital of carbon.

To determine the overall properties of the spin defects in the hBN-defect array, we also measure the other color-center defects. Our method includes a brightness threshold (here, it is chosen as 0.5 MHz under 100- μ W laser excitation), which excludes the dark emission centers directly. We detect 20 emission points that are beyond the brightness threshold in the hBN array. All of their emissions exhibit an antibunching effect, and 17 of them exhibit a measurable ODMR signal with an external longitudinal magnetic field, suggesting a high yield of 85%. As the comparison, we investigate the probability of finding such defects in directly spin-coated samples using the same brightness threshold. Fifty bright points are investigated, and only 2 of them are found to exhibit both an antibunching effect and an ODMR signal. The probability is 4%. Detailed data are shown in Table 2. Therefore, our method of creating an isolated-hBN-flake array and setting a brightness threshold enhances the success probability by 21-fold. We also perform Rabi oscillation measurements for all the isolated defects found with ODMR, and only 2 are revealed to have distinct Rabi oscillations, displaying a relatively low probability of demonstrating coherent control (~10.5%). Considering this low probability, the 21-fold enhancement induced by our method is critical to observing the coherent control of a single spin at room temperature.

In Supplementary Note 4, we present the measurement results of some of the bright spots in the array sample. Most of these defects exhibit similar optical properties (ZPL at 540 ± 10 nm) and spin signals (a positive ODMR contrast and the same position of the ODMR peak at the same magnetic field). Therefore, we speculate that they are the same type of defect, which is intrinsic in the hBN powder with a relatively low probability but can be found effectively using our method. During the measurements, we also find some other phenomena; for example, we observe the hyperfine structure of a single spin defect and a relatively high ODMR contrast (~7%) of another defect, which may be contributed to other new found defects (see Supplementary Note 6).

In conclusion, we report and characterize a new type of ultrabright single spin defect in hBN and demonstrate the room-temperature quantum control of the hBN single spin, owing to our method of creating an isolated-hBN-flake array and setting a brightness threshold, which enhances the success probability of finding an isolated defect with an ODMR signal by 21-fold. The spin defects of hBN exhibit excellent quantum emission properties and significant coherent-spin characteristics. This defect may be a complex of carbon and oxygen dopants according to our ab initio calculations. The room-temperature quantum control of the single spin in hBN combined with its good optical properties is a crucial step toward utilizing two-dimensional-material spin in quantum-information applications.

Methods

Sample preparation

A silicon wafer with 280-nm thermally-grown SiO₂ on top is first cleaned by ultrasonication with acetone, isopropanol and deionized water in sequence. Then the pattern of the MW waveguide is formed on the wafer coated with positive S1813 resists by photolithography. A 100-nm gold film is coated on the wafer by an e-beam evaporator, and the extra gold is

stripped by heating in N-Methylpyrrolidone (NMP) to form the gold film MW waveguide. Subsequently, 300-nm positive PMMA resist is spun onto the wafer and baked. Arrays of circular holes 520-nm in diameter are patterned into the PMMA on the gold film using 100-keV electron beam lithography. HBN ultrafine powders with 99.0% purity⁴¹ and ~70 nm particle size are obtained commercially from Graphene Supermarket and annealed in high vacuum at 1000 °C for 2 hours. A small amount of hBN nanopowder is mixed in ultrapure water and sonicated into a suspension. A drop of suspension is placed on the edge of the wafer, and then the slide attached to the wafer is slowly moved to disperse the droplets into the holes. Finally, the PMMA resists are dissolved in acetone, leaving arrays of hBN on the gold-film MW waveguide.

Fitting of optical propriety data

The experimental $g^{(2)}(\tau)$ data can be fitted well using the three-level Model $g^{(2)}(\tau) = 1 - (1+a)e^{-|\tau|/\tau_1} + ae^{-|\tau|/\tau_2}$, where a is a fitting parameter and τ_1 and τ_2 are the lifetimes of excited and metastable states, respectively⁴⁴. This model indicates the existence of a metastable state, which is essential for room-temperature spin polarization and optical detection of spin resonance⁵⁴. The radiative lifetime $\tau_1 \sim 2.5$ ns is consistent with that previously reported, and the nonradiative lifetime τ_2 is much longer (~600 ns) at 100- μ W laser power. The emission polarization is fitted by $e_1 + e_2 \cos^2(\theta + e_3)$, where e_1 , e_2 , and e_3 are the fitting parameters, and θ is the polarization angle of the emitted fluorescence. The DOP (~0.8) is derived by $e_2/(2e_1 + e_2)$. The experimental data of PL count versus excitation power are fitted by the Equation $I = I_{\text{sat}} \times P/(P + P_{\text{sat}})$, where I_{sat} is the saturated emission rate and P_{sat} is the saturation power. $I_{\text{sat}} = 3.7 \pm 0.20$ MHz and $P_{\text{sat}} = 446 \pm 54$ μ W.

Theoretical simulation

The ab initio density functional theory (DFT) calculations were carried out within the Vienna ab initio simulation package (VASP)^{55,56}. The projector augmented wave (PAW) formalism^{57,58} is used to describe the electron and spin density near the nuclei. An 8 × 8 bulk hexagonal supercell with 256 atoms is constructed by embedding the point defects. The modified screened hybrid density functional of Heyd, Scuseria, and Ernzerhof (HSE)⁵⁹ is used to relax the structure and calculate the electronic properties. We increase the exact nonlocal Hartree-Fock exchange ($\alpha = 0.32$) with the generalized gradient approximation of Perdew, Burke, and Ernzerhof (PBE)⁶⁰. The convergence criteria of total energy and quantum mechanical forces on the atoms are set to 10^{-5} eV and 0.01 eV/Å with a plane wave cutoff energy of 450 eV. The Brillouin-zone is sampled by the single Γ -point scheme. The optimized interlayer distance was 3.37 Å with the DFT-D3 method of Grimme⁶¹ for dispersion correction. The excited states were calculated by the Δ SCF method^{62–64}. The cw ODMR spectra can be calculated by the EASYSIN toolbox based on the hyperfine matrix from DFT calculations⁶⁵. Here, the nuclear Zeeman and quadrupole interactions are not considered⁴⁵.

Data availability

The data that support the findings of this study are available within the article and its Supplementary Information. Additional relevant data are available from the corresponding authors upon reasonable request.

Code availability

The code used in this study is available from the corresponding authors upon reasonable request.

References

1. Wolfowicz, G. et al. Quantum guidelines for solid-state spin defects. *Nat. Rev. Mater.* **6**, 906–925 (2021).
2. Doherty, M. W. et al. The nitrogen-vacancy colour centre in diamond. *Phys. Rep.* **528**, 1–45 (2013).
3. Lohrmann, A., Johnson, B. C., McCallum, J. C. & Castelletto, S. A review on single photon sources in silicon carbide. *Rep. Prog. Phys.* **80**, 034502 (2017).
4. Awschalom, D. D., Hanson, R., Wrachtrup, J. & Zhou, B. B. Quantum technologies with optically interfaced solid-state spins. *Nat. Photon.* **12**, 516–527 (2018).
5. Atatüre, M., Englund, D., Vamivakas, N., Lee, S.-Y. & Wrachtrup, J. Material platforms for spin-based photonic quantum technologies. *Nat. Rev. Mater.* **3**, 38–51 (2018).
6. Aharonovich, I., Englund, D. & Toth, M. Solid-state single-photon emitters. *Nat. Photon.* **10**, 631–641 (2016).
7. Schirhagl, R., Chang, K., Loretz, M. & Degen, C. L. Nitrogen-vacancy centers in diamond: nanoscale sensors for physics and biology. *Annu. Rev. Phys. Chem.* **65**, 83–105 (2014).
8. Bernien, H. et al. Heralded entanglement between solid-state qubits separated by three metres. *Nature* **497**, 86–90 (2013).
9. Caldwell, J. D. et al. Photonics with hexagonal boron nitride. *Nat. Rev. Mater.* **4**, 552–567 (2019).
10. Grosso, G. et al. Tunable and high-purity room temperature single-photon emission from atomic defects in hexagonal boron nitride. *Nat. Commun.* **8**, 1–8 (2017).
11. Liu, W. et al. An ultrastable and robust single-photon emitter in hexagonal boron nitride. *Physica E Low Dimens. Syst. Nanostruct.* **124**, 114251 (2020).
12. Tetienne, J. P. Quantum sensors go flat. *Nat. Phys.* **17**, 1074–1075 (2021).
13. Liu, Y. et al. Van der Waals heterostructures and devices. *Nat. Rev. Mater.* **1**, 1–17 (2016).
14. Gottscholl, A. et al. Initialization and read-out of intrinsic spin defects in a van der Waals crystal at room temperature. *Nat. Mater.* **19**, 540–545 (2020).
15. Kianinia, M., White, S., Froch, J. E., Bradac, C. & Aharonovich, I. Generation of spin defects in hexagonal boron nitride. *ACS Photonics* **7**, 2147–2152 (2020).
16. Gao, X. et al. Femtosecond laser writing of spin defects in hexagonal boron nitride. *ACS Photonics* **8**, 994–1000 (2021).
17. Murzakhanov, F. F. et al. Creation of negatively charged boron vacancies in hexagonal boron nitride crystal by electron irradiation and mechanism of inhomogeneous broadening of boron vacancy-related spin resonance lines. *Nanomaterials* **11**, 1373 (2021).
18. Guo, N.-J. et al. Generation of spin defects by ion implantation in hexagonal boron nitride. *ACS Omega* **7**, 1733–1739 (2022).
19. Ivády, V. et al. Ab initio theory of the negatively charged boron vacancy qubit in hexagonal boron nitride. *Npj Comput. Mater.* **6**, 41 (2020).
20. Reimers, J. R. et al. Photoluminescence, photophysics, and photochemistry of the V_B^- defect in hexagonal boron nitride. *Phys. Rev. B* **102**, 144105 (2020).
21. Baber, S. et al. Excited state spectroscopy of boron vacancy defects in hexagonal boron nitride using time-resolved optically detected magnetic resonance. *Nano Lett.* **22**, 461–467 (2021).
22. Mathur, N. et al. Excited-state spin-resonance spectroscopy of V_B^- defect centers in hexagonal boron nitride. *Nat. Commun.* **13**, 3233 (2022).
23. Yu, P. et al. Excited-state spectroscopy of spin defects in hexagonal boron nitride. *Nano Lett.* **22**, 3545–3549 (2022).
24. Mu, Z. et al. Excited-state optically detected magnetic resonance of spin defects in hexagonal boron nitride. *Phys. Rev. Lett.* **128**, 216402 (2022).
25. Liu, W. et al. Temperature-dependent energy-level shifts of spin defects in hexagonal boron nitride. *ACS Photonics* **8**, 1889–1895 (2021).
26. Gottscholl, A. et al. Spin defects in hBN as promising temperature, pressure and magnetic field quantum sensors. *Nat. Commun.* **12**, 4480 (2021).
27. Chejanovsky, N. et al. Single-spin resonance in a van der Waals embedded paramagnetic defect. *Nat. Mater.* **20**, 1079–1084 (2022).
28. Mendelson, N. et al. Identifying carbon as the source of visible single-photon emission from hexagonal boron nitride. *Nat. Mater.* **20**, 321–328 (2021).
29. Stern, H. L. et al. Room-temperature optically detected magnetic resonance of single defects in hexagonal boron nitride. *Nat. Commun.* **13**, 618 (2022).
30. Gao, X. et al. High-contrast plasmonic-enhanced shallow spin defects in hexagonal boron nitride for quantum sensing. *Nano Lett.* **21**, 7708–7714 (2021).
31. Gottscholl, A. et al. Room temperature coherent control of spin defects in hexagonal boron nitride. *Sci. Adv.* **7**, eabf3630 (2021).
32. Liu, W. et al. Coherent dynamics of multi-spin V_B^- center in hexagonal boron nitride. *Nat. Commun.* **13**, 5713 (2022).
33. Frösch, J. E. et al. Coupling spin defects in hexagonal boron nitride to monolithic bullseye cavities. *Nano Lett.* **21**, 6549–6555 (2021).
34. Mendelson, N. et al. Coupling spin defects in a layered material to nanoscale plasmonic cavities. *Adv. Mater.* **34**, 2106046 (2021).
35. Preuß, J. A. et al. Assembly of large hBN nanocrystal arrays for quantum light emission. *2D Mater.* **8**, 035005 (2021).
36. Malaquin, L., Kraus, T., Schmid, H., Delamarche, E. & Wolf, H. Controlled particle placement through convective and capillary assembly. *Langmuir* **23**, 11513–11521 (2007).
37. Cui, Y. et al. Integration of colloidal nanocrystals into lithographically patterned devices. *Nano Lett.* **4**, 1093–1098 (2004).
38. Cassabois, G., Valvin, P. & Gil, B. Hexagonal boron nitride is an indirect bandgap semiconductor. *Nat. Photon* **10**, 262–266 (2016).
39. Weng, Q. et al. Tuning of the optical, electronic, and magnetic properties of boron nitride nanosheets with oxygen doping and functionalization. *Adv. Mater.* **29**, 1700695 (2017).
40. Bourrellier, R. et al. Bright UV single photon emission at point defects in h-BN. *Nano Lett.* **16**, 4317–4321 (2016).
41. Chen, Y. et al. Solvent-exfoliated hexagonal boron nitride nanoflakes for quantum emitters. *ACS Appl. Nano Mater.* **4**, 10449–10457 (2021).
42. Jungwirth, N. R. et al. Temperature dependence of wavelength selectable zero-phonon emission from single defects in hexagonal boron nitride. *Nano Lett.* **16**, 6052–6057 (2016).
43. Tran, T. T. et al. Robust multicolor single photon emission from point defects in hexagonal boron nitride. *ACS Nano* **10**, 7331–7338 (2016).
44. Tran, T. T., Bray, K., Ford, M. J., Toth, M. & Aharonovich, I. Quantum emission from hexagonal boron nitride monolayers. *Nat. Nanotechnol.* **11**, 37–41 (2016).
45. Auburger, P. & Gali, A. Towards ab initio identification of paramagnetic substitutional carbon defects in hexagonal boron nitride acting as quantum bits. *Phys. Rev. B* **104**, 075410 (2021).
46. Li, S. & Gali, A. Identification of an oxygen defect in hexagonal boron nitride. *J. Phys. Chem. Lett.* **13**, 9544–9551 (2022).
47. Smart, T., Li, K., Xu, J. & Ping, Y. Intersystem crossing and exciton-defect coupling of spin defects in hexagonal boron nitride. *Npj Comput. Mater.* **7**, 1–8 (2021).
48. Weston, L., Wickramaratne, D., Mackoite, M., Alkauskas, A. & Walle, C. Native point defects and impurities in hexagonal boron nitride. *Phys. Rev. B* **97**, 214104 (2018).

49. Li, K., Smart, T. & Ping, Y. Carbon trimer as a 2 eV single-photon emitter candidate in hexagonal boron nitride: A first-principles study. *Phys. Rev. Mater.* **6**, 042201 (2022).
50. Li, S., Pershin, A., Thiering, G., Udvarhelyi, P. & Gali, A. Ultraviolet quantum emitters in hexagonal boron nitride from carbon clusters. *J. Phys. Chem. Lett.* **13**, 3150–3157 (2022).
51. Jara, C. et al. First-principles identification of single photon emitters based on carbon clusters in hexagonal boron nitride. *J. Phys. Chem. A* **125**, 1325–1335 (2021).
52. Maciaszek, M., Razinkovas, L. & Alkauskas, A. Thermodynamics of carbon point defects in hexagonal boron nitride. *Phys. Rev. Mater.* **6**, 014005 (2022).
53. Berseneva, N., Krasheninnikov, A. & Nieminen, R. Mechanisms of postsynthesis doping of boron nitride nanostructures with carbon from first-principles simulations. *Phys. Rev. Lett.* **107**, 035501 (2011).
54. Widmann, M. et al. Coherent control of single spins in silicon carbide at room temperature. *Nat. Mater.* **14**, 164–168 (2015).
55. Kresse, G. & Furthmüller, J. Efficiency of ab-initio total energy calculations for metals and semiconductors using a plane-wave basis set. *Comput. Mater. Sci.* **6**, 15–50 (1996).
56. Kresse, G. & Furthmüller, J. Efficient iterative schemes for ab initio total-energy calculations using a plane-wave basis set. *Phys. Rev. B* **54**, 11169 (1996).
57. Blöchl, P. Projector augmented-wave method. *Phys. Rev. B* **50**, 17953 (1994).
58. Kresse, G. & Joubert, D. From ultrasoft pseudopotentials to the projector augmented-wave method. *Phys. Rev. B* **59**, 1758 (1999).
59. Heyd, J., Scuseria, G. & Ernzerhof, M. Hybrid functionals based on a screened coulomb potential. *J. Chem. Phys.* **118**, 8207–8215 (2003).
60. Perdew, J., Burke, K. & Ernzerhof, M. Generalized gradient approximation made simple. *Phys. Rev. Lett.* **77**, 3865 (1996).
61. Grimme, S., Antony, J., Ehrlich, S. & Krieg, H. A consistent and accurate ab initio parametrization of density functional dispersion correction (DFT-D) for the 94 elements H-Pu. *J. Chem. Phys.* **132**, 154104 (2010).
62. Gali, A., Janzén, E., Deák, P., Kresse, G. & Kaxiras, E. Theory of spin-conserving excitation of the N-V⁻ center in diamond. *Phys. Rev. Lett.* **103**, 186404 (2009).
63. Wu, Q. & Van Voorhis, T. Direct optimization method to study constrained systems within density-functional theory. *Phys. Rev. A* **72**, 024502 (2005).
64. Alkauskas, A., Buckley, B., Awschalom, D. & Walle, C. First-principles theory of the luminescence lineshape for the triplet transition in diamond NV centres. *New J. Phys.* **16**, 073026 (2014).
65. Stoll, S. & Schweiger, A. EasySpin, a comprehensive software package for spectral simulation and analysis in EPR. *J. Magn. Reson.* **178**, 42–55 (2006).

Acknowledgements

This work is supported by the Innovation Program for Quantum Science and Technology (No. 2021ZD0301200), the National Natural Science Foundation of China (Nos. 12174370, 11904356, 12174376, and 11821404), the Youth Innovation Promotion Association of Chinese Academy of Sciences (No. 2017492), the Open Research Projects of

Zhejiang Lab (No. 2021MBOABO2), the Fok Ying-Tong Education Foundation (No. 171007). This work was partially carried out at the USTC Center for Micro and Nanoscale Research and Fabrication. A.G. acknowledges the Hungarian NKFIH grant No. KKP129866 of the National Excellence Program of Quantum-coherent materials project and the support for the Quantum Information National Laboratory from the Ministry of Innovation and Technology of Hungary, and the EU H2020 project QuanTelCo (Grant No. 862721).

Author contributions

N.-J.G., W.L., Y.-T.W., J.-S.T., Y.-Z.Y., and X.-D.Z. conceived the experiments and analyzed the data with discussion of S.Y., Y.M., Q.L., J.-F.W., J.-S.X., R.-C.G., and G.-C.G. N.-J.G., Y.-Z.Y., and X.-D.Z. performed the experiments with assistance of Z.-P.L., Z.-A.W., and L.-K.X. S.L. and A.G. conceived and carried out the theoretical simulations. N.-J.G. W.L., Y.-T.W., J.-S.T., and S.L. wrote the manuscript. C.-F.L., A.G., and J.-S.T. supervised and coordinated the project.

Competing interests

The authors declare no competing interests.

Additional information

Supplementary information The online version contains supplementary material available at <https://doi.org/10.1038/s41467-023-38672-6>.

Correspondence and requests for materials should be addressed to Yi-Tao Wang, Jian-Shun Tang, Adam Gali or Chuan-Feng Li.

Peer review information *Nature Communications* thanks Tongcang Li, and the other, anonymous, reviewers for their contribution to the peer review of this work.

Reprints and permissions information is available at <http://www.nature.com/reprints>

Publisher's note Springer Nature remains neutral with regard to jurisdictional claims in published maps and institutional affiliations.

Open Access This article is licensed under a Creative Commons Attribution 4.0 International License, which permits use, sharing, adaptation, distribution and reproduction in any medium or format, as long as you give appropriate credit to the original author(s) and the source, provide a link to the Creative Commons license, and indicate if changes were made. The images or other third party material in this article are included in the article's Creative Commons license, unless indicated otherwise in a credit line to the material. If material is not included in the article's Creative Commons license and your intended use is not permitted by statutory regulation or exceeds the permitted use, you will need to obtain permission directly from the copyright holder. To view a copy of this license, visit <http://creativecommons.org/licenses/by/4.0/>.

© The Author(s) 2023